This manuscript has been submitted for publication in **Earth and Planetary Science Letters**. Please note that, the manuscript is still undergoing peer-review, the manuscript has yet to be for formally accepted for publication. Subsequent versions of this manuscript may have different contents, depending on reviewers' comments. If accepted, the final version of this manuscript will be available via the 'Peer-reviewed Publication DOI' link on the right-hand side of this webpage. Please feel free to contact any of the authors; we welcome feedback.

Spatial characteristics and kinematics of precession-driven floodplain aggradation cycles in the lower Eocene Willwood Formation of the Bighorn Basin, Wyoming, USA

Youwei Wang[1], Timothy F. Baars[1], Joep E.A. Storms[1], Allard W. Martinius[1,2], Philip D. Gingerich[3], Magda Chmielewska[4], Simon J. Buckley[5], and Hemmo A. Abels[1]*

[1] Department of Geosciences and Engineering, Delft University of Technology, Stevinweg 1, 2628 CN Delft, the Netherlands

[2] Equinor ASA, Arkitekt Ebbellsvei 10, N–7053 Trondheim, Norway

[3] Museum of Paleontology, University of Michigan, Ann Arbor, MI 48109-1079, USA

[4] Department of Geology and Petroleum Geology, University of Aberdeen, Aberdeen AB24 3UE, UK

[5] NORCE Norwegian Research Centre AS, P.O. Box 22, N-5838 Bergen, Norway

**Correspondence email: y.wang.delft@outlook.com*

Abstract:

Interaction of allogenic and autogenic forcing in building alluvial stratigraphy remains a complex subject that is critical for paleoenvironmental and paleoclimate reconstruction and subsurface rock property prediction. Astronomical forcing of alluvial stratigraphy is poorly documented so far as this driver strongly interacts with autogenic and other allogenic processes making it difficult to trace astronomical climate changes in these laterally highly variable sediments. In the lower Eocene Willwood Formation, Bighorn Basin, Wyoming, USA, a lot of evidence has been gathered to relate dominant floodplain aggradation cycles to precession-scale climate change. One floodplain aggradation cycle consists of two phases: (1) a longer overbank phase with relative channel stability and strong paleosol development on fine clastic sediments; and (2) a shorter avulsion phase characterized by channel instability and weak to no pedogenesis on heterolithic sandy avulsion-belt deposits. Previous studies have analyzed these cycles to be consistently developed in multiple areas of the basin of different ages and, in one study, in two parallel one-dimensional (1-D) stratigraphic sections spaced several kilometers apart. However, the 3-D geometry of floodplain aggradation cycles remains largely unknown, which determines to what extent allogenic climate forcing produces regionally consistent sedimentary patterns and autogenic processes produce lateral variability. Here, 44 floodplain aggradation cycles were mapped and measured in 3-D using an unmanned aerial vehicle (UAV) to develop a photogrammetric model covering a geographic area of ~10 km^2 and spanning a stratigraphic succession of ~300 m. The 44 cycles have an average thickness of 6.8 m with a standard deviation of 2.0 m, which is in line with previous studies. Most cycles are consistently traceable over the entire model, indicating spatial consistency and in line with allogenic climate forcing by the astronomical precession cycle. Individual floodplain aggradation cycles may change in thickness rapidly when traced laterally, with rates up to 1 m over a lateral distance of 100 m and a maximum of 4 m. Detailed mapping of seven successive cycles reveals differences in their regionally-averaged thicknesses of 3.7 m to 9.7 m, with their coefficients of variation ranging between 17% and 28%. Variogram analysis demonstrates that the thickness of a cycle at one locality is statistically related to that at another locality over an average distance of 1.3 km in the paleoflow direction and 0.6 km perpendicular to the paleoflow direction. These different directional trends are interpreted to result from morphological elements oriented in paleoflow directions in the fluvial landscapes shaping more consistency of the sedimentary elements in paleoflow direction. Two different metrics suggest that full-compensational stacking occurs after deposition of 6 to 7 cycles, or timescales of ca. 120 to 140 kyr, although strong thickness compensation is shown to start at the subsequent one and two floodplain aggradation cycles, so at ca. 20-40 kyr time scales.

Keywords: precession; floodplain aggradation cycle; compensational stacking; alluvial stratigraphy; Eocene; Bighorn Basin

1. INTRODUCTION

Alluvial stratigraphy is fundamentally controlled by channel avulsion frequency and long-term sediment accumulation rates (Allen, 1978; Ashworth *et al.*, 2004) that are recorded by the distribution and configuration of channel sandstone bodies and coeval fine-grained sediment (Allen, 1978; Bridge & Leeder, 1979). Channel avulsion is an important process in channelized depositional systems. Channels aggrade or prograde faster than surrounding non-channelized regions (Hajek & Wolinsky, 2012), causing avulsion to occur when a topographic threshold is exceeded (Karssenberg & Bridge, 2008; Mohrig *et al.*, 2000). A difference is made between local and regional avulsion (Slingerland & Smith, 2004). A local avulsion may be triggered by simple channel blockage and has a local impact with the channel moving back into the original channel further downstream if that trajectory remains energetically most advantageous.

The rates at which superelevation is reached depend on channel belt and floodplain aggradation rates as well as non-deposition or degradation rates that are different between channel belts and floodplains. Rates of aggradation or degradation depend on accommodation and sediment supply. Superelevation may be reached with all settings stable due to continuous higher aggradation rates in the channel belts than in the floodplains. River avulsions in these cases are fully autogenically controlled. Climate, tectonics, and base level may also impact these factors and speed up or slow down the rates at which superelevation is reached.

Fluvial aggradational cycles have been reported in the Cretaceous-Paleogene of West Texas (Atchley *et al.*, 2004), the Triassic of New Mexico (Cleveland *et al.*, 2007), and the Eocene of northern Wyoming (Kraus, 1987; Abels *et al.*, 2013). These cycles are meter-scale, with typically fining-upward successions. They generally consist of two phases: (1) an overbank phase with relative channel stability and strong paleosol development on fine clastic sediments; and (2) an avulsion phase characterized by channel instability and weak to no pedogenesis on heterolithic sandy avulsion-belt deposits (Abels *et al.*, 2013).

Most fluvial aggradational cycles are reported to be driven by base-level variations possibly in combination with upstream climatic or tectonic changes, but they may be fully autogenic in nature as well. The floodplain aggradation cycles in the Eocene Willwood Formation of the Bighorn Basin in northern Wyoming cannot be driven by the base-level change as that is reported to be stable over time (Foreman *et al.*, 2012), which is attributed to the fact that the Bighorn Basin is an intermontane basin with no direct sea/lake-level connection. Instead, these cycles are reported to be driven by precession-scale climate change in multiple studies by indicating their duration to be around 20 kyr (Abdul Aziz *et al.*, 2008; Abels *et al.*, 2013; Van der Meulen *et al.*, 2020).

Previous Bighorn Basin Eocene studies have characterized and dated these cycles of different ages in various 1-D stratigraphic sections, including cycles in parallel sections separated by several kilometers (Abdul Aziz *et al.*, 2008; Abels *et al.*, 2013; Westerhold *et al.*, 2018; van der Meulen *et al.*, 2020). However, their 3-D characteristics have not been studied. Lateral consistency of allogenically-driven cycles is expected, as external climate change would influence the whole basin at the same time. Local processes such as channel migration, local splaying, and avulsions are, however, expected to be an integral part of the dynamic fluvial environment and thus cause lateral and vertical variability on top of the regionally-consistent stratigraphy driven by external climate forcing. The spatial and temporal scales at which these local, autogenic processes act and interact with regional, allogenic processes remain unknown, but crucial when these fluvial records are used for paleoenvironmental and paleoclimatic reconstructions (Straub & Foreman, 2018) and when the subsurface fluvial record is being interpreted and/or predicted.

Here, we, therefore, analyze the precession-driven floodplain aggradation cycles in continuous outcrops of the lower Eocene Willwood Formation in the McCullough Peaks area of the Bighorn Basin, Wyoming, to reveal their spatial consistency and variability and to elucidate the spatial and temporal scales at which autogenic and allogenic controls interact and dominate. The objectives of this study are fourfold: (1) to investigate the traceability of floodplain aggradation cycles over a larger lateral distance; (2) to reveal the regionally-average vertical thicknesses and variability among individual cycles through the stratigraphy; (3) to characterize the lateral variability within each cycle; and (4) to evaluate compensational stacking through temporally-successive cycles. Finally, we aim to kinematically understand the fluvial morphodynamics that drive the dominant alluvial stratigraphy in the basin.

2. GEOLOGICAL SETTING

The Bighorn Basin is a Laramide intermontane basin with a drainage outlet opening to the north (Fig. 1; Abels *et al.*, 2013). It hosts one of the best-studied terrestrial successions for fluvial cyclicity, with much research carried out on paleosols and river avulsion deposits (Neasham & Vondra, 1972; Bown & Kraus, 1981; Kraus & Aslan, 1993; Abels *et al.*, 2013; Foreman *et al.*, 2012; Owen *et al.*, 2017; and many others). Lower Eocene sediments exhibit regular alternations that have been related to the autogenic behavior that is intrinsic in a fluvial depositional system (Clyde & Christensen, 2003) and to allogenic forcing that is extrinsic (Kraus & Aslan, 1993; Abdul Aziz *et al.*, 2008; Abels *et al.*, 2013). Red/purple/grey paleosols are strikingly consistent over a large lateral extent, with dominant type I paleosols, a few type II paleosols, and rare type III paleosols (Kraus, 2002). These paleosols are products of the overbank phase, and they alternate with heterolithic deposits representing avulsion (Abels *et al.*, 2013). The paleoenvironments and paleoclimates in the basin have been extensively studied from floral and faunal fossils (Gingerich, 2010). The mammal stratigraphy and data collections provide an accurate stratigraphy within the frame of the other stratigraphic controls as magnetostratigraphy, chemostratigraphy, and tephrastratigraphy (Clyde *et al.*, 1994; Gingerich, 2010).

The McCullough Peaks study area is in the northwestern part of the Bighorn Basin (Fig. 1) and comprises an area of relatively large exposures of basinal sediments. The study interval here represents about 0.9 Myr of geological time straddling the interval in which the Eocene Thermal Maximum 2 and subsequent H2 events occur (Abels *et al.*, 2016). The lower boundary is approximately 55 Ma, so about 1 Myr younger than the Paleocene-Eocene boundary marked by the Paleocene-Eocene Thermal Maximum (PETM; Koch *et al.*, 1992). Fluvial strata in the study area have a dominant paleoflow direction of NNW to NNE (Neasham & Vondra, 1972).

3. METHODOLOGY

3.1 Field survey

Stratigraphic sections were measured by digging 0.5-1 m wide and 0.5-1 m deep trenches down to fresh rock. Field units were designated based on field estimation of grain size; matrix color; abundance, size, and color of mottling; presence, abundance, and size of carbonate nodules; and abundance and size of slickensides. Hand sampling and field descriptions followed methods detailed in the Soil Survey Manual (Soil Survey Division Staff, 1993). Five long trenches were logged, with three reported in Abels *et al.* (2012, 2013, 2016) and two reported here (see Fig. 2 for their locations). Palaeocurrent directions were measured from dune-scale cross-stratification (mainly planar and trough cross-stratification) in channelized sandstone bodies.

3.2 UAV-based photogrammetry

Photographs were taken automatically every three seconds by a 20-megapixel camera mounted on a multirotor unmanned aerial vehicle (UAV; DJI Phantom 4 Pro). The UAV was flown parallel to the outcrop surface manually at a speed of 5-10 m/s to provide a 60% horizontal overlap between successive photos. Each outcrop area was photographed from at least three different heights with different camera angles to provide complete coverage and to aid alignment during processing.

The final model includes 21144 photos taken on 34 flights (Fig. 2), and it covers a total area of ~10 km^2, with approximate north-south and east-west lengths of 2.5 km and 4 km, respectively. The studied stratigraphic succession is ~300 m thick and dips at ~2° towards the south. Fifty-seven ground control points (GCPs) were placed (Fig. 2) and surveyed using an Emlid Reach GNSS receiver, hereinafter referred to as the rover. Accuracy of GCPs was improved by using the Post-Processed Kinematic (PPK) positioning technique which compares the rover-recorded GCP position to a second Emlid Reach GNSS receiver that acted as a stationary local base station. Both the rover and base station recorded raw GNSS measurements, which were then processed using the open-source GNSS post-processing package RTKLIB. The position of the base station was calibrated by collecting several hours of data and running the PPK solution against the nearest public Continuous Operating Reference Station (CORS) based in Fishtail, Montana (P722). The GCP positions were then determined with centimeter accuracy relative to the local base station.

Agisoft PhotoScan (Version 1.4.3, July 2018; current Metashape) was used to build the 3-D digital models (virtual outcrops) from the acquired georeferenced photos, using the structure from motion multi-view stereo (SfM-MVS) photogrammetric method (Eltner *et al.*, 2016). Three-dimensional point clouds were generated in the Universal Transverse Mercator (UTM) coordinate system. Finally, a triangulated digital surface mesh was created, and the photos were draped onto the surface as the texture. Due to the large size of the area mapped, the complete photogrammetric image set was split into 42 model sections. For each section, a tiled model was generated (Buckley *et al.*, 2008), allowing the entire 3-D outcrop model to be imported into LIME (version 2.2.2; Buckley *et al.*, 2019) for visualization and interpretation.

3.3 Cycle boundary identification

Cycle boundary tops are placed at the sharpest facies transition from red/purple paleosols to whitish heterolithic deposits (Fig. S1). This is slightly different from the procedure of Abels *et al.* (2013) who put cycle boundaries at the sharpest transition in the soil development index (SDI) curve, which often corresponds to the top of the reddest soil. The cycle boundary of this study is in most cases slightly higher (0.6 m on average and up to 3.5 m for the seven cycles shown in Fig. S1) than that of Abels *et al.* (2013). The reason for the chosen strategy is the impossibility to calculate SDI without non-weathered rock surface descriptions from trenched sections. Interpretation in the photogrammetric model is started from trenched sections (see their localities in Fig. 2), where fresh rock descriptions are available. During this process, UAV- and hand-held camera-captured photos are used to aid interpretation where the model resolution is not sufficiently high.

3.4 Variogram analysis

As widely used to quantify variables in space, the variogram is a function of variance over lag distance h, with larger variogram values corresponding to longer lag distances (Fig. S2). A variogram can be calculated as follows (Pyrcz & Deutsch, 2003):

$$\gamma(\mathrm{h}) = \frac{1}{2N(h)}\sum_{\alpha=1}^{N(h)}(z(u_\alpha) - z(u_\alpha + h))^2 \quad (1)$$

where $\gamma(\mathrm{h})$ is a measure of dissimilarity between two data points over lag distance h; $N(h)$ is the number of data point pairs; u_α is a data point at location α in 2-D space; $u_\alpha + h$ is a data point separated from u_α by the distance h; $z(u_\alpha)$ is the numerical value at data point u_α; and $z(u_\alpha + h)$ is the numerical value at location $u_\alpha + h$.

Cycle thicknesses are measured on outcrop surfaces in the model every 20 meters, which could be impossible at some locations due to vegetation, low model resolution, and recent debris. These thickness measurements are then analyzed as a 2-D directional variogram using Python codes by Pyrcz (2020). Variograms are calculated in six directions that separate 180° into six equal azimuth zones (e.g. 0°, 30°, 60°, 90°, 120°, and 150°) after observation of any statistical anisotropy in the variogram map. The lag distance is set as 100 m, with a lag tolerance of 50 m. The search strategy utilizes a wide azimuth tolerance (30°) and a large bandwidth (2 km) to reduce the nugget effect near the origin (Zhang *et al.*, 2005). In a directional variogram, a range is identified when the sill ($\gamma(h) = 1$) is reached (Fig. S2). Within the range, the cycle thickness at one locality is stochastically related to that at another locality, which is referred to as the spatial continuity of the cycle thickness. Such continuity is expected to be the largest in the paleoflow direction according to Pyrcz & Deutsch (2014).

3.5 Compensational stacking analysis

3.5.1 Coefficient of variation

The coefficient of variation (CV) is defined as the ratio of the standard deviation over the mean, and thus a smaller CV indicates less variability. If the thickness of a stratigraphic unit like a floodplain aggradation cycle has a small CV, then the thickness of the unit has a relatively even distribution throughout the area. To investigate compensational stacking, successive cycles are combined as a stratigraphic unit to calculate CV. Seven successive cycles with high lateral coverage in the model, labelled as cycles H to N, are selected for this analysis. In practice, a CV is first calculated for the thickness of one cycle (e.g., cycle H), followed by calculation of a CV for the thickness of two successive cycles combined (e.g., cycles H and I), then three successive cycles (e.g., cycles H, I, and J), …, and finally a CV for all of the available cycles combined.

3.5.2 Compensational stacking index

The standard deviation of sedimentation/subsidence (σ_{ss}) (Wang *et al.*, 2011) can be used to characterize the compensational timescale:

$$\sigma_{ss}(T) = \left\{ \int_0^L \left[\frac{r(T;x)}{\hat{r}(x)} - 1 \right]^2 dL \right\}^{1/2} \tag{2}$$

where $r(T;x)$ is the average deposition rate at a horizontal coordinate of x during a time interval of T, L is the cross-basin length, and $\hat{r}(x)$ is the local long-term sedimentation (or subsidence) rate.

Empirically, σ_{ss} is expected to decrease as T increases, following a power-law trend (Equation 3, Straub *et al.*, 2009; Wang *et al.*, 2011):

$$\sigma_{ss} = a'T^{-\kappa} \tag{3}$$

where a' is a coefficient, and κ is termed the compensation index. At a certain time scale when κ exceeds 1.0, the stratigraphic stacking is purely compensational (Straub *et al.*, 2009).

However, it is impossible to make many long 1-D sections that span the whole stratigraphy due to the limitation of outcrop exposure and the presence of sandstone bodies and vegetation. With this metric, the compensational stacking is explored using only one 1-D composite section.

4. RESULTS

4.1 Floodplain aggradation cycle traceability and composite stratigraphy

A total of 44 cycles are identified throughout the studied ~300-m stratigraphy in the model, and their boundaries are well recognizable stratigraphically and traceable laterally. Local factors might hinder lateral tracing, such as occurrences of channel sandstone bodies, splitting or merging of soil horizons at the stratigraphic interval of the recognized boundary, recent debris and vegetation over the outcrops, and the low resolution of the photogrammetric model in some places due to lower overlap of UAV-images or larger distances at which these were taken causing lower resolution. Figure 3 shows how these cycle boundaries are traced in the photogrammetric model.

The stratigraphy in which the 44 cycles are recognized starts 7 cycles below the base of the Deer Creek Amphitheater section of Abels *et al.* (2013) and ends at/above the top of the Upper Deer Creek section of Abels *et al.* (2012) and Creek Star Hill section of Abels *et al.* (2016). The lower 10 cycles and upper 11 cycles have limited lateral extents within the photogrammetric model. Most of the other cycles can be traced over a maximum distance of 4 km in the NE-SW direction and ~2.5 km in the SE-NW direction. A composite section that includes all of the 44 cycles is constructed by combining available trenched sections (DCA and UDC sections; Abels *et al.* 2012, 2016). We have extended the cycle labelling system of Abels *et al.* (2013) and Abels *et al.* (2012) rather than starting a new one (see Fig. 4A). Cycles P1 to P3 correspond to the hyperthermal ETM2 and cycles P5 to P8 correspond to the hyperthermal H2 (Abels *et al.* 2012, 2016; Fig. 1).

The composite stratigraphy with 44 floodplain aggradation cycles has a cumulative thickness of ~300 m (Fig. 4A), which is based on 1-D data and thus no regional averages of cycle thicknesses are included. The thickness of individual cycles ranges between 3.4 m and 12.5 m, with an average of 6.8 m and a standard deviation of 2.0 m (Fig. 4B).

4.2 Lateral thickness variability of individual floodplain aggradation cycles

Detailed mapping of cycles H to N shows that individual thickness measurements range between 2 m and 18 m with CV ranging between 17% and 28% (Fig. 5), and regional average thicknesses of cycles H to N vary between 3.7 m (cycle K) and 9.7 m (cycle L). The average of all cycle thicknesses is 7.3 m with a standard deviation of 2.6 m (Fig. 5). These numbers are comparable to those calculated for all 44 cycles in the 1-D composite section (6.8 ± 2.0 m, Fig. 4B) and previously reported values.

We make a total of 22 digital sections in the photogrammetric model, such as section 14 (S14) in Figure 3B. In these sections, the seven cycles studied in detail are complete and free of channelized sandstone bodies. The top cycles are flattened in Figure 6, in which cycle thicknesses vary rapidly in the lateral direction, with a maximum of 4 m over a distance of 400 m.

Variograms are calculated for the seven cycles to indicate the correlativity of the cycle thickness at one specific location to that at another over a certain distance. The correlatable distance is on average 1.3 km in the long-range direction (see its definition in Section 3.4) and 0.6 km in the short-range direction (Fig. 7A and Table S1). The aspect ratio of the variogram ellipse varies between 1.4 to 5.3, with an average of 2.2 (Table S1). The long-range azimuth ranges between 310° and 80°, averaging 1° (Fig. 7B and Table S1), which coincides with the average paleoflow direction measured in the dune-scale cross-beddings in the field (4° ± 24°; Fig. 7C). Individual 1-D variograms show repetitive, non-monotonic features (e.g. Fig. 8B), which are referred to as cyclicity by Pyrcz & Deutsch (2003). Meanwhile, there are also non-monotonic variograms that don't present repetitive patterns (e.g. Fig. 8E), which, together with the above-mentioned cyclicity, are referred to as the hole effect (cf. Pyrcz & Deutsch, 2003).

4.3 Vertical floodplain aggradation cycle stacking

A locally thicker floodplain aggradation cycle seemingly tends to stack on a locally thinner cycle and vice versa. Examples are the thicker-than-average cycle L and the thinner-than-average cycle M in Section S18 of Figure 6. To quantify this compensational stacking behaviour, two metrics are used. For the first metric, we compile the thicknesses of individual cycles and divide the thickness by their average. Now, the standard deviation of each cycle thickness is equivalent to its CV since the average is 1. Subsequently, the CV of two successive cycles at individual locations as a stratigraphic unit is calculated (Fig. 9). This shows a significantly reduced CV from 23% to 14%, a reduction of 53% of the total CV reduction (numerically calculated as $\frac{23\% - 14\%}{23\% - 6\%}$). Stacking three cycles at individual locations reduces the CV by 76% to 10%. The CV does not decrease further than 6% when 6 successive cycles are stacked.

For the second metric, we calculate σ_{ss} using the composite section shown in Figure 4A based on the method described in Section 3.5.2. The predicted compensational timescale is identified by drawing two trend lines representing best-fit linear regression of the dots before and after the knick point. Thus, the predicted compensational timescale corresponds to 7 cycles, although the slopes on both sides of the knick point are quite similar. According to the method, this indicates stratigraphic stacking becomes fully compensational after deposition of 7 cycles (Fig. 9).

5. DISCUSSION

5.1 Fluvial aggradational cycles – Lateral Consistency

Floodplain aggradation cycles are dominant features of alluvial stratigraphy in many alluvial records (Kraus and Aslan, 1997; Abels *et al.*, 2013; Atchley *et al.*, 2013). They are related to phases of river stability and deposition of true overbank fines on which strong paleosols may develop and phases of regional-scale river avulsion causing deposition of the heterolithic avulsion belt on which weak or no soils develop (Kraus and Aslan, 1993; Abels *et al.*, 2013). In the Bighorn Basin, the floodplain aggradation cycles have been linked to precession-scale climate change (Abdul Aziz *et al.*, 2008; Abels *et al.*, 2013, 2016; Van der Meulen *et al.*, 2020) although the climatic model remains enigmatic (Abels *et al.*, 2013).

At least six different stratigraphic sections of three different intervals of time in the Bighorn Basin have now revealed similarly-thick floodplain aggradation cycles (Abdul Aziz *et al.*, 2008, Abels *et al.*, 2013, 2016; Westerhold *et al.*, 2019; Van der Meulen *et al.*, 2020). Previously, lateral consistency was only demonstrated in two 1-D parallel sections spaced 7.5 km with correlations confirmed by carbon isotopes (Van der Meulen *et al.*, 2020). Consistency over 15 km was suggested by Westerhold *et al.* (2018), which, however, could not be independently confirmed by stratigraphic constraints. Here, we demonstrate lateral consistency of individual cycles over a 10 km^2 area and a maximum length of 4 km approximately in the paleoflow direction. We also demonstrate floodplain aggradation cycles to be a consistent component of alluvial stratigraphic build-up over nearly 1 Myr in the lower Eocene Willwood Formation with 44 cycles stacking to make ~300 m stratigraphy. The lateral consistency of floodplain aggradation cycles found in this study, the continuity of these cycles in stratigraphy in line with all available dating that suggests their occurrences at precession-time scales, and all previous documentation of cyclicity, strongly confirm their allogenic nature.

Longer-term aggradation rates depend on the accommodation creation, which, in the case of the Bighorn Basin where sea/lake-level variation is absent, is related to tectonic subsidence. Abels *et al.* (2013) argued that reaching superelevation was likely at pace with the accommodation creation by tectonic subsidence and precession-driven climate changes. This means that the long-term average floodplain aggradation cycle thickness would approach the long-term basin subsidence. If all these 44 cycles with an average thickness of 6.8 m are driven by precession cycles with a duration of ca. 20 kyr, the estimated basin subsidence rate equivalent to the long-term sedimentation rate would be ~0.34 m/ky. This is in line with previous estimates of 0.29-0.39 m/kyr (Clyde *et al.*, 1994; Westerhold *et al.*, 2007; Stap *et al.*, 2009; Gingerich, 2010; Abels *et al.*, 2012, 2013). Also, subsidence rates and aggradation rates were relatively constant over long periods of time, as suggested by previous research based on stable carbon isotope dating (Abels *et al.*, 2016). At the Paleocene-Eocene transitional interval, floodplain aggradation cycles are reported to be slightly thicker, reaching an average of 8 m per cycle (Abdul Aziz *et al.*, 2008; Van der Meulen *et al.*, 2020). This may indicate a long-term reduction of tectonic subsidence during the early Eocene (Abels *et al.*, 2016; Van der Meulen *et al.*, 2020).

In numerical forward model runs, Wang *et al.* (2021) found that very short forcing cycle wavelengths may render channel belts unable to reach superelevation in time, and thus not all individual forcing cycles can cause regional avulsion phases, but instead, avulsion phases occur every second, third, or fourth cycle. These authors also found that very-long forcing cycle wavelengths may cause the superelevation to be reached in the overbank phase and thus accelerate the entrance of the system into the avulsion phase. There may however be a range of intermediate wavelengths, where the system maintains its behavior for some time until the trigger occurs. The balance between subsidence, sedimentation, and climate change time scales, may in that sense be less critically exactly coinciding. Instead, the fluvial systems may maintain themselves at a certain state for some time, slowly building up stratigraphy; fluvial changes may occur if a strong climate trigger occurs during that time.

It remains enigmatic what climate triggers produce the floodplain aggradation cycles in the Willwood Formation. Likely, this had to do with sediment supply, both amount and type, and discharge hydrograph. Wang *et al.* (2021) produce regional avulsion and overbank phases in a diffusion-based numerical forward stratigraphic model. In their model, increasing sediment supply relative to water discharge causes sediment accumulation in the channel belt and speeds up the time to superelevation, after which regional-scale avulsion occurs. In comparison, during the interval of decreasing sediment supply relative to water discharge, the channel belts are incisive and overbank deposition occurs (Wang *et al.*, 2021). Within the Bighorn Basin, climate changes may have also strongly impacted groundwater levels and vegetation types and intensity, which may also play important roles.

The average thickness of 44 stacked floodplain aggradation cycles in the 1-D section (6.8 m) and that of 7 successive cycles that are mapped in the whole 3-D space (7.3 m) are quite similar. However, the seven detailedly mapped cycles show different thicknesses also when averaged over the entire width of the study area. We think this can be because of two different reasons. The first is that not all precession cycles are of the same wavelength. Typically, insolation curves show intervals of more pronounced cyclicity in the vicinity of eccentricity maxima and intervals of less pronounced cyclicity in the vicinity of eccentricity minima. In the latter parts, obliquity often plays a more important role (Abels *et al.*, 2009). Also, precession frequencies are more than a simple 20-kyr sine wave (Berger *et al.*, 1992). This causes variability in the forcing and thus may drive thicker and thinner cycles in terms of the regional average thicknesses (Fig. 5) in response to shorter or longer insolation cycles. But, second, we cannot yet know whether the spatial consistency and variability of floodplain aggradation cycles recorded in our study area (~10 km^2) is indeed a regional-scale representation. Thinner cycles may display thickening features outside the study area. We think the current size of the study area is large enough to deduce conclusions about lateral consistency and variability of the cycles, but we cannot exclude that (slightly) different numbers pop up when larger areas are analyzed.

5.2 Fluvial aggradational cycles – Lateral Variability

Thicknesses of individual floodplain aggradation cycles may change rapidly in the lateral direction with rates up to 4 m over a lateral distance of 400 m (Fig. 6). It should be noted that all of the geometries discussed here are derived from compacted stratigraphy. Part of the variability that is measured likely relates to differential compaction between different lithologies. We did attempt to decompact the series and reconstruct these differential thicknesses but we were so far unsuccessful, as we found out this requires detailed information on early-stage consolidation and later-stage compaction and the exact rates of these. Differential early-stage consolidation may cause higher or lower sedimentation in different areas and thus influence the subsequent thicknesses of stratigraphy, while late-stage compaction does not impact sedimentation. We envision that a backstripping exercise with active sedimentation and thus knowledge about rates of sedimentation depending on topography is needed to decompact the succession and reconstruct the paleotopography. That is clearly beyond the scope of the current work. Therefore, all the results we present and discuss are of compacted stratigraphy.

The thickness variability at local scales is obvious for all the seven cycles detailed mapped within the 10 km^2 study area, and this is related here to morphologic variability within the fluvial system in combination with differential compaction as discussed above. Morphologic elements in the fluvial landscape are major and minor channel belts, crevasse splays, levees, and floodplains. These caused different rates and types of sedimentation in different areas, which thereby resulted in topographic gradients between them. Major channels elevate above the landscape just before avulsion and the sands receive little consolidation afterward compared to the clays of the surrounding floodplains. With that, major and to some extent likely minor sandbodies will result in topographic highs in the subsequent cycles causing less sediment to arrive at those locations. Thicker-than-average cycles at some localities are more often dominated by crevasse splay sediments, and their overlying sediments are finer and more often dominated by distal floodplain soils. How this results in compensational stacking will be discussed in Section 5.3. Typically, such lateral morphological changes and related consolidation differences explain the thickness variations of floodplain aggradation cycles.

The spatial continuity of the cycle thicknesses is stronger in the direction of paleoflow than that perpendicular to paleoflow (Fig. 7). This could be indicative of how floodplain deposits are morphologically segmented by single or stacked channels oriented into the downstream direction. Moreover, the morphological effect of channel segmentation could depend on the fluvial styles, as the number of river threads and the frequency of flooding and splaying will impact floodplain variability. The cyclicity and the hole effect found in the variogram analysis (Fig. 8) could be related to channel-segmented blocks that are expressed as depressions or topographic highs (cf. Pyrcz & Deutsch, 2003).

We analyze, using similar methods, the numerically-modelled stratigraphy in the KB08 model of Wang *et al.* (2021). In their Scenario A40, water discharge and sediment input are fed cyclically with a wavelength of 10 kyr and an amplitude of 40%, which produces four cycles that mimic those in the Bighorn Basin. Variogram analysis is implemented using the thickness map of the third fluvial aggradation cycle in the center of the basin to avoid the too strong impact of either upstream or downstream factors (Fig. 10). Interestingly, we find a long range of 22 km in the direction of paleoflow and a short range of 6 km perpendicular to paleoflow in the cross-basin direction (Fig. 10D). The hole effect is also present (e.g., azimuths 30° and 120° in Fig. 10D), which have similar characters to those based on the field data (Fig. 8). It should be noted that the modelled strata are free of compaction while the field counterparts are not. The hole effect seems to be related to the presence of various depressions such as the blue low-thickness areas in Figure 10C or topographic highs such as the red/yellow high-thickness areas in Figure 10C. The lows and highs in modelled stratigraphy result from the segmentation of floodplain fines by channel belts that represent the finest resolution of the numerical model and could represent channels in the field. The similarity between the numerical model and the field data in terms of variogram features might indicate similar spatial features of floodplain aggradation cycles as shaped by the (modelled/real) fluvial processes.

5.3 Compensational stacking of floodplain sedimentation

Compensational stacking refers to the tendency of a depositional system to fill the gaps and remove the highs in topography (Straub *et al.*, 2009; Straub and Pyles, 2012). In other words, relatively high or low topography in the local areas will lead to local higher deposition or erosion rates during the formation of subsequent and overlying floodplain aggradation cycles. Therefore, compensational stacking is expected to significantly reduce the topographic differences if the depositional time is sufficiently long, which means the smoothing effect of the later deposited cycle is much larger than the newly introduced morphological variability. Several other factors are also influential, in particular the early consolidation effect that may result in variable topography that was originally flat but had different soil characters. For example, sandstone bodies remain highs in the landscape as these consolidate less, while floodplain clay or even peat eventually produce lows in the landscape as these relatively consolidate more. Therefore, we attribute the compensational stacking found in this study to be the result of both fluvial morphology and compaction. In section 5.2, we have discussed why decompaction at these scales has been unfeasible within the current study.

Two metrics (i.e., CV and σ_{ss}) point to full compensational timescales corresponding to 6 and 7 floodplain aggradation cycles (i.e., ~120-140 kyr), respectively. However, 54% compensational stacking is already reached in the subsequent first cycle and 76% in the subsequent two cycles. The remaining 23% compensational stacking occurs when the stacked cycle number increases from 3 to 6 (CV drops from 9% to 6%). These numbers are similar, while they are based on different methods applied to different datasets. The CV metric is based on measurements of the lateral thickness data of seven cycles in 22 digital sections over the whole study area, whereas the compensational index method is based on a long 1-D composite section lacking lateral data. The CV metric is favored because of the underlying 3-D dataset, but it comprises a limited stratigraphic interval. The compensational index method is based on a very long sedimentary record (~300 m), but it is applied in a 1-D dataset instead of a 3-D one. Therefore, the timescales we obtain here await examination by both spatially wider and stratigraphically longer datasets.

The compensational timescales corresponding to 6 or 7 precession cycles are longer than those identified in previous research, such as ~2.0 kyr modelled timescale in the fully autogenic numerical scenario of Wang *et al.* (2020) as well as the 67 kyr, 100 kyr, and 55 kyr timescales based on the estimation of the maximum channel belt sandstone body thickness and the long-term sedimentation rate in the Bighorn Basin, Piceance Creek Basin, and Trem-Graus Basin (Straub *et al.*, 2020). This difference can be explained by the fact that the basic stratigraphic units used in our study are different from those in the aforementioned studies. Straub *et al.* (2020) use decennial to centennial-scale intervals as their basic stratigraphic units, which implies the availability of high-resolution data, while we use precession-driven floodplain aggradation cycles as the basic stratigraphic units, which implies low-resolution data. This finding is in line with the argument of Straub & Pyles (2012) that compensational stacking is prevalent at various hierarchical scales. Straub & Pyles (2012) pinpointed that units as small as individual channel beds are compensating the topographic differences created by older beds, whereas units of channel stories and higher hierarchy (i.e. channel element and channel complex) are also compensating during their stacking. Nonetheless, the compensational timescales identified in this study and other studies are not universally applicable for all basins that record precession-scale cyclicity, since it depends on several site-specific factors, such as sediment supply, basin size and slope, base-level fluctuation, and subsidence-caused accommodation changes. Moreover, we also find that considerable, though not full, compensational stacking already occurs as the subsequent floodplain aggradation cycles get deposited, which is evidenced by the sharp reduction of CV from 23% to 14% (Fig. 9). Furthermore, Wang et al. (2021) showed that the compensational timescale in an allogenically-involved scenario (5.1 kyr; C10 and C20 with wavelengths of 10 kyr) is about 2.6 times of that in the fully autogenic scenario (2.0 kyr), which indicates the interference of allogenic forcing on autogenic processes.

5.4 Disentangling autogenic and allogenic drivers of floodplain sedimentation

One of the goals of this study has been to disentangle allogenic from autogenic sedimentation in the alluvial succession of the Bighorn Basin. With the laterally-consistent, precession-driven floodplain aggradation cycles, the successions display a strong impact of allogenic, cyclic forcing. Local, automated processes, such as splaying or avulsion and minor distributaries, interplay with this external forcing. With the study of the lateral consistency and variability, we think we have demonstrated that allogenic and autogenic forcing may eventually indeed be separated to some extent. Some of the spatial and temporal impacts of both allogenic and autogenic controls have also been quantified here. These are the lateral continuity of geometry in paleoflow and perpendicular to paleoflow and the rates of lateral thickness changes and maximum thickness changes of the cycles.

The separation and quantification of allogenic and autogenic variability in the fluvial stratigraphy of the Bighorn Basin display examples from a single case. The specific size of the morphological elements in that fluvial system will determine the spatial scale of autogenic variability in the rock record together with the activity of these elements. The dominance of this autogenic variability in the stratigraphic record will be determined by the aggradation rates. High aggradation rates will cause the imprints of autogenic variability to be spread through the record, while low aggradation rates will cause single levels to be dominated by autogenic variability. As such, floodplain aggradation cycles will be less visible in those low-aggradation settings. On the other hand, in high accumulation-rate settings, external drivers like cyclic climate forcing may be better displayed in the stratigraphic record. However, to what extent autogenic processes will start to act also at these longer timescales if allogenic triggers remain absent, remains unknown.

6. CONCLUSIONS

We here study the interaction of allogenic climate forcing and autogenic processes on building alluvial stratigraphy of the lower Eocene Willwood Formation, Bighorn Basin, Wyoming. The local floodplain stratigraphy is dominated by floodplain aggradation cycles, recognized in many successions globally, and in this basin thought to be controlled by precession-scale climate change. Analysis of a fully-georeferenced 3-D photogrammetric model covering an area of ~10 km^2 and a succession thickness of ~300 m in the McCullough Peaks Area of the Bighorn Basin reveals a total of 44 stacked floodplain aggradation cycles. These cycles display an average thickness of 6.8 m and a standard deviation of 2.0 m. We find a strong lateral consistency of the floodplain aggradation cycles and a solid continuity in stratigraphy in line with all available dating that suggests the occurrence of these cycles at precession-time scales. These findings, together with all previous documentation of cyclicity in the study area, strongly confirm their allogenic, precession-driven nature. Meanwhile, these floodplain aggradation cycles display a strong lateral thickness variability that is ascribed to autogenic processes in the fluvial system. Cycle thickness may change as rapidly as 1 m over 100 m when traced laterally, with a maximum of 4 m. Variogram analysis shows that the thickness of an individual cycle at a specific locality is related to that at another locality over an average distance of 1.3 km in the paleoflow direction and 0.6 km perpendicular to the paleoflow direction. We attributed this to the more continuous morphodynamic features of a fluvial system in the paleoflow direction, thereby indicating the decisive role of fluvial dynamics in shaping geological bodies. The major part of the compensational stacking of stratigraphy occurs after the deposition of 3 floodplain aggradation cycles, while full compensation seems to be reached after 6 to 7 cycles. The regional traceability of and variability among individual cycles as well as spatial continuity and variability within individual cycles provide an example of the interaction between allogenic and autogenic controls on alluvial stratigraphy and the opportunity to disentangle the impact of these processes in the rock record.

ACKNOWLEDGEMENTS

This study was financially supported by Top Sectors GeoEnergie, Equinor, and Wintershall to HAA, JEAS, AWM, and TFB (FRESCO Project, Grant No. TKI2018–03–GE), a China Scholarship Council grant to YW (No. 201606440046), the Dutch Molengraaff fund to YW (Stichting Molengraaff Fonds), and the IAS/SEPM travel grants to YW that indirectly contributes to the 2019 field visit. The authors acknowledge the help from Chaowen Wang, Dirk-Jan Walstra, Hiranya Sahoo, and the Churchill family of Wyoming for help and encouragement in the field, Jasper de Lanoy for the earlier photogrammetric model interpretations, and Suihong Song for discussion on variogram analysis.

REFERENCES

Abdul Aziz, H., **Hilgen, F.J.**, **van Luijk, G.M.**, **Sluijs, A.**, **Kraus, M.J.**, **Pares, J.M.** and **Gingerich, P.D.** (2008) Astronomical climate control on paleosol stacking patterns in the upper Paleocene–lower Eocene Willwood Formation, Bighorn Basin, Wyoming. *Geology*, **36**, 531–534.

Abels, H.A., **Clyde, W.C.**, **Gingerich, P.D.**, **Hilgen, F.J.**, **Fricke, H.C.**, **Bowen, G.J.** and **Lourens, L.J.** (2012) Terrestrial carbon isotope excursions and biotic change during Palaeogene hyperthermals. *Nat. Geosci.*, **5**, 326–329.

Abels, H.A., **Kraus, M.J.** and **Gingerich, P.D.** (2013) Precession-scale cyclicity in the fluvial lower Eocene Willwood Formation of the Bighorn Basin, Wyoming (USA). *Sedimentology*, **60**, 1467–1483.

Abels, H.A., **Lauretano, V.**, **van Yperen, A.E.**, **Hopman, T.**, **Zachos, J.C.**, **Lourens, L.J.**, **Gingerich, P.D.** and **Bowen, G.J.** (2016) Environmental impact and magnitude of paleosol carbonate carbon isotope excursions marking five early Eocene hyperthermals in the Bighorn Basin, Wyoming. *Clim. Past*, **12**, 1151–1163.

Allen, J.R.L. (1978) Studies in fluviatile sedimentation: an exploratory quantitative model for the architecture of avulsion-controlled alluvial suites. *Sediment. Geol.*, **21**, 129–147.

Ashworth, P.J., **Best, J.L.** and **Jones, M.** (2004) Relationship between sediment supply and avulsion frequency in braided rivers. *Geology*, **32**, 21.

Atchley, S.C., **Nordt, L.C.** and **Dworkin, S.I.** (2004) Eustatic Control on Alluvial Sequence Stratigraphy: A Possible Example from the Cretaceous-Tertiary Transition of the Tornillo Basin, Big Bend National Park, West Texas, U.S.A. *J. Sediment. Res.*, **74**, 391–404.

Berger, A., **Loutre, M.F.** and **Laskar, J.** (1992) Stability of the Astronomical Frequencies Over the Earth's History for Paleoclimate Studies. *Science*, **255**, 560–566.

Birgenheier, L., **Vanden Berg, M.**, **Plink-Bjorklund, P.**, **Gall, R.**, **Rosencrans, E.**, **Rosenberg, M.J.**, **Toms, L.C.** and **Morris, J.** (2019) Climate impact on fluvial-lake system evolution, Eocene Green River Formation, Uinta Basin, Utah, USA. GSA Bull. doi: 10.1130/B31808.1

Bridge, J.S. and **Leeder, M.R.** (1979) A simulation model of alluvial stratigraphy. *Sedimentology*, **26**, 617–644.

Buckley, S.J., **Ringdal, K.**, **Naumann, N.**, **Dolva, B.**, **Kurz, T.H.**, **Howell, J.A.** and **Dewez, T.J.B.** (2019) LIME: Software for 3-D visualization, interpretation, and communication of virtual geoscience models. *Geosphere*, **15**, 222–235.

Buckley, S.J., **Vallet, J.**, **Braathen, A.** and **Wheeler, W.** (2008) Oblique helicopter-based laser scanning for digital terrain modelling and visualisation of geological outcrops. *Int. Arch. Photogramm. Remote Sens. Spat. Inf. Sci.*, **37 (B4)**, 493–498.

Cleveland, D.M., **Atchley, S.C.** and **Nordt, L.C.** (2007) Continental Sequence Stratigraphy of the Upper Triassic (Norian Rhaetian) Chinle Strata, Northern New Mexico, U.S.A.: Allocyclic and Autocyclic Origins of Paleosol-Bearing Alluvial Successions. *J. Sediment. Res.*, **77**, 909–924.

Clyde, W., **Stamatakos, J.** and **Gingerich, P.** (1994) Chronology of the Wasatchian Land-Mammal Age (Early Eocene): Magnetostratigraphic Results from the McCullough Peaks Section, Northern Bighorn Basin, Wyoming. J Geol. doi: 10.1086/629680

Clyde, W.C. and **Christensen** (2003) Testing the relationship between pedofacies and avulsion using Markov analysis. *Am. J. Sci.*, **303**, 60–71.

Eltner, A., **Kaiser, A.**, **Castillo, C.**, **Rock, G.**, **Neugirg, F.** and **Abellan, A.** (2016) Image-based surface reconstruction in geomorphometry - merits, limits and developments. *Earth Surf. Dyn.*, **4**, 359–389.

Finn, T.M., Kirschbaum, M.A., Roberts , S.B., Condon, S.M., Roberts, L.N.R.,and Johnson, R.C. (2010) Cretaceous–Tertiary Composite Total Petroleum System (503402), Bighorn Basin, Wyoming and Montana, *U.S. Geological Survey Digital Data Series DDS-69-V*, 157 p.

Foreman, B.Z., **Heller, P.L.** and **Clementz, M.T.** (2012) Fluvial response to abrupt global warming at the Palaeocene/Eocene boundary. *Nature*, **491**, 92–95.

Gingerich, P. D. (2010) Mammalian faunal succession through the Paleocene-Eocene thermal maximum (PETM) in western North America**.** *Vertebrata PalAsiatica*, **48**, 308–327**.**

Hajek, E.A. and **Wolinsky, M.A.** (2012) Simplified process modeling of river avulsion and alluvial architecture: Connecting models and field data. *Sediment. Geol.*, **257–260**, 1–30.

Karssenberg, D. and **Bridge, J.S.** (2008) A three-dimensional numerical model of sediment transport, erosion and deposition within a network of channel belts, floodplain and hill slope: extrinsic and intrinsic controls on floodplain dynamics and alluvial architecture. *Sedimentology*, **55**, 1717–1745.

Koch, P., **Zachost, J.C.** and **Gingericht, P.D.** (1992) Correlation between isotope records in marine and continental carbon reservoirs near the Palaeocene/Eocene boundary. **358**, 4.

Kraus, M.J. (1987) Integration of channel and floodplain suites, II. Vertical relations of alluvial paleosols. *J. Sed. Petrol.*, **57**, 602–612.

Kraus, M.J. (2002) Basin-Scale changes in floodplain paleosols: implications for interpreting alluvial architecture. *J. Sediment. Res.*, **72**, 500–509.

Kraus, M.J. and **Aslan, A.** (1993) Eocene hydromorphic paleosols: significance for interpreting ancient floodplain processes. SEPM J Sediment Res. doi: 10.1306/D4267B22-2B26-11D7-8648000102C1865D

Mohrig, D., **Heller, P.L.**, **Paola, C.** and **Lyons, W.J.** (2000) Interpreting avulsion process from ancient alluvial sequences: Guadalope-Matarranya system (northern Spain) and Wasatch Formation (western Colorado). *Geol. Soc. Am. Bull.*, 17.

Neasham, J.W. and **Vondra, C.F.** (1972) Stratigraphy and Petrology of the Lower Eocene Willwood Formation, Bighorn Basin, Wyoming. *Geol. Soc. Am. Bull.*, **83**, 2167.

Owen, A., **Ebinghaus, A.**, **Hartley, A.J.**, **Santos, M.G.M.** and **Weissmann, G.S.** (2017) Multi-scale classification of fluvial architecture: An example from the Palaeocene-Eocene Bighorn Basin, Wyoming. *Sedimentology*, **64**, 1572–1596.

Pyrcz, M. (2020). GitHub repository, https://github.com/GeostatsGuy/

Pyrcz, M. and **Deutsch, C. V.** (2003) The whole story on the hole effect. *Geostatistical Association of Australasia, Newsletter*, **18**.

Pyrcz, M. and **Deutsch, C.V.** (2014) Geostatistical reservoir modeling, Second edition. *New York, New York : Oxford University Press*, Oxford, 433 pp.

Slingerland, R. and **Smith, N.D.** (2004) RIVER AVULSIONS AND THEIR DEPOSITS. *Annu. Rev. Earth Planet. Sci.*, **32**, 257–285.

Soil Survey Division Staff (1993) Soil Survey Manual, vol. 18. Soil Conservation Service, U.S. Department of Agriculture, USA.

Stap, L., **Sluijs, A.**, **Thomas, E.** and **Lourens, L.** (2009) Patterns and magnitude of deep sea carbonate dissolution during Eocene Thermal Maximum 2 and H2, Walvis Ridge, southeastern Atlantic Ocean. Paleoceanography. doi: https://doi.org/10.1029/2008PA001655

Straub, K.M., **Duller, R.A.**, **Foreman, B.Z.** and **Hajek, E.A.** (2020) Buffered, Incomplete, and Shredded: The Challenges of Reading an Imperfect Stratigraphic Record. J Geophys Res Earth Surf. doi: 10.1029/2019JF005079

Straub, K.M. and **Foreman, B.Z.** (2018) Geomorphic stasis and spatiotemporal scales of stratigraphic completeness. *Geology*, **46**, 311–314.**Straub, K.M.**, **Paola, C.**, **Mohrig, D.**, **Wolinsky, M.A.** and **George, T.** (2009) Compensational Stacking of Channelized Sedimentary Deposits. *J. Sediment. Res.*, **79**, 673–688.

Straub, K.M. and **Pyles, D.R.** (2012) Quantifying the Hierarchical Organization of Compensation In Submarine Fans Using Surface Statistics. *J. Sediment. Res.*, **82**, 889–898.

van der Meulen, B., **Gingerich, P.D.**, **Lourens, L.J.**, **Meijer, N.**, **van Broekhuizen, S.**, **van Ginneken, S.** and **Abels, H.A.** (2020) Carbon isotope and mammal recovery from extreme greenhouse warming at the Paleocene–Eocene boundary in astronomically-calibrated fluvial strata, Bighorn Basin, Wyoming, USA. *Earth Planet. Sci. Lett.*, **534**, 116044.

Wang, C., **Adriaens, R.**, **Hong, H.**, **Elsen, J.**, **Vandenberghe, N.**, **Lourens, L.J.**, **Gingerich, P.D.** and **Abels, H.A.** (2017) Clay mineralogical constraints on weathering in response to early Eocene hyperthermal events in the Bighorn Basin, Wyoming (Western Interior, USA). *Geol. Soc. Am. Bull.*, **129**, 997–1011.

Wang, Y., **Storms, J.E.A.**, **Martinius, A.W.**, **Karssenberg, D.** and **Abels, H.A.** (2021) Evaluating alluvial stratigraphic response to cyclic and non-cyclic upstream forcing through process-based alluvial architecture modelling. *Basin Res.*, **33**, 48–65.

Wang, Y., **Straub, K.M.** and **Hajek, E.A.** (2011) Scale-dependent compensational stacking: An estimate of autogenic time scales in channelized sedimentary deposits. *Geology*, **39**, 811–814.

Westerhold, T., **Röhl, U.**, **Laskar, J.**, **Raffi, I.**, **Bowles, J.**, **Lourens, L.J.** and **Zachos, J.C.** (2007) On the duration of magnetochrons C24r and C25n and the timing of early Eocene global warming events: Implications from the Ocean Drilling Program Leg 208 Walvis Ridge depth transect. Paleoceanography. doi: https://doi.org/10.1029/2006PA001322

Westerhold, T., **Röhl, U.**, **Wilkens, R.H.**, **Gingerich, P.D.**, **Clyde, W.C.**, **Wing, S.L.**, **Bowen, G.J.** and **Kraus, M.J.** (2018) Synchronizing early Eocene deep-sea and continental records – cyclostratigraphic age models for the Bighorn Basin Coring Project drill cores. *Clim. Past*, **14**, 303–319.

Zhang, Y., **Person, M.**, **Paola, C.**, **Gable, C.W.**, **Wen, X.-H.** and **Davis, J.M.** (2005) Geostatistical analysis of an experimental stratigraphy: geostatistical analysis of experimental stratigraphy. Water Resour Res. doi: 10.1029/2004WR003756

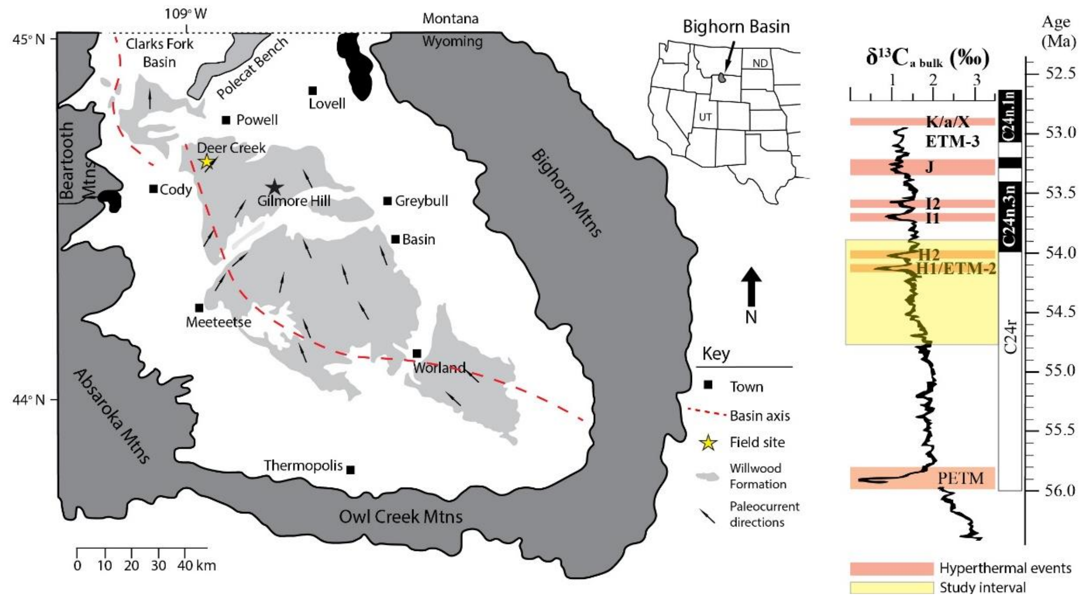

Figure 1. The left panel shows the location of the study area, the McCullough Peaks, in the northern Bighorn Basin, Wyoming (after Wang *et al.*, 2018), with basin axis following Finn et al. (2010). The right stratigraphic column shows the study interval, which is modified after Birgenheier *et al.* (2019).

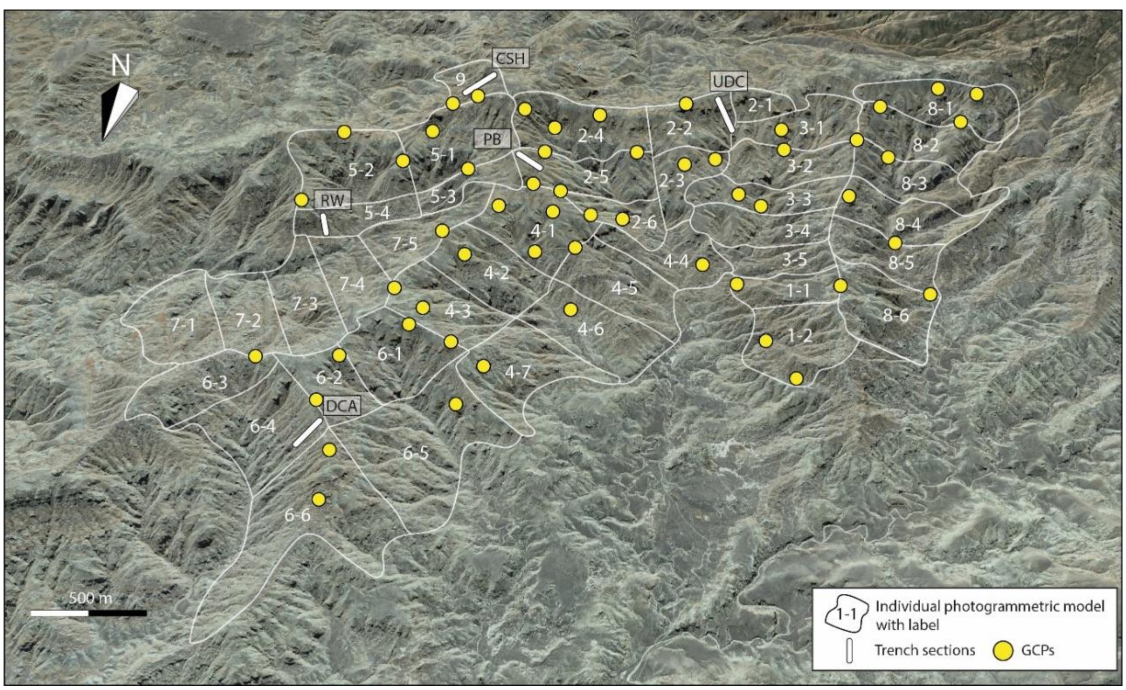

Figure 2. A bird's eye view from Google Earth showing the coverage of 42 individual photogrammetric 3-D models. Abbreviations: DCA--Deer Creek Amphitheater section (Abels *et al.*, 2013), PB--Purple Butte section, UDC--

Upper Deer Creek section (Abels *et al.*, 2012), CSH--Creek Star Hill section (Abels *et al.*, 2016), and RW--Roan Wash section.

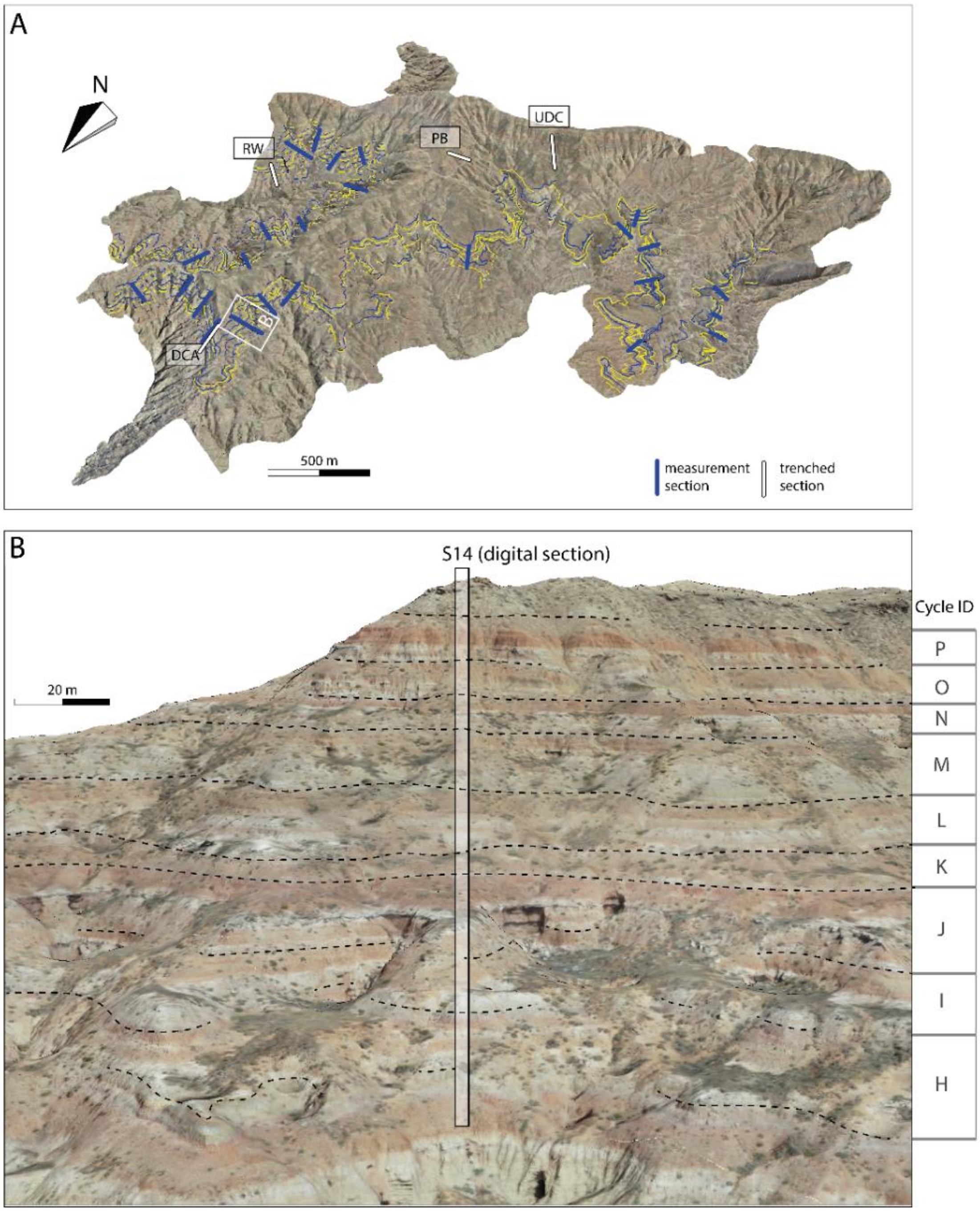

Figure 3. Tracing of floodplain aggradation cycles in the photogrammetric model with the aid of individual drone and camera photos. (A) An overview of the interpreted 3-D photogrammetric model in the McCullough Peaks area,

showing traced boundaries for seven successive cycles. (B) A zoomed-in outcrop section in the 3-D model, showing how cycle boundaries (blue and yellow lines) are traced and how a digital section (S14) is constructed.

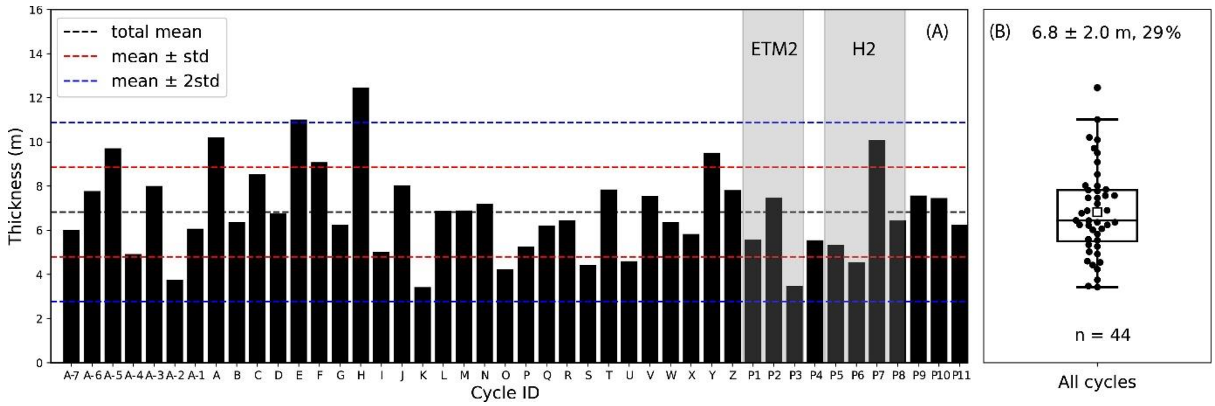

Figure 4. Thicknesses of 44 cycles in the composite stratigraphy. (A) Bar diagram showing the labeling system and cycle thickness variability. (B) Boxplot showing the mean (6.8 m), standard deviation (2.0 m), and CV (standard deviation/mean; 29%) of thicknesses of these 44 cycles. Box boundaries indicate lower and upper quartiles, lines extending from boxes represent the 1st to 2nd and 3rd to 4th quartile ranges, lines and squares within boxes indicate median and mean values, and points outside boxes stand for outliers.

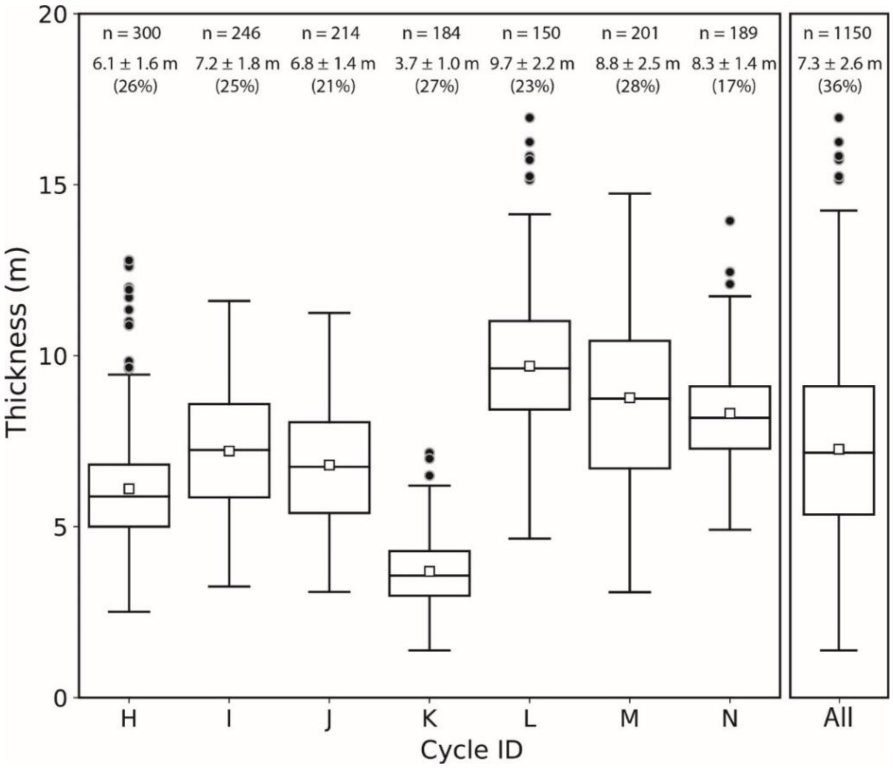

Figure 5. Box plots illustrating the variability of the thicknesses of cycles H-N. The very right boxplot is based on 1150 measurements that are equally contributed by the seven cycles by randomly selecting 150 measurements from each cycle. See explanations of boxplot components in Figure 6. Note that: the number combination of "a ± b (c)" above each boxplot means "average ± standard deviation (CV)".

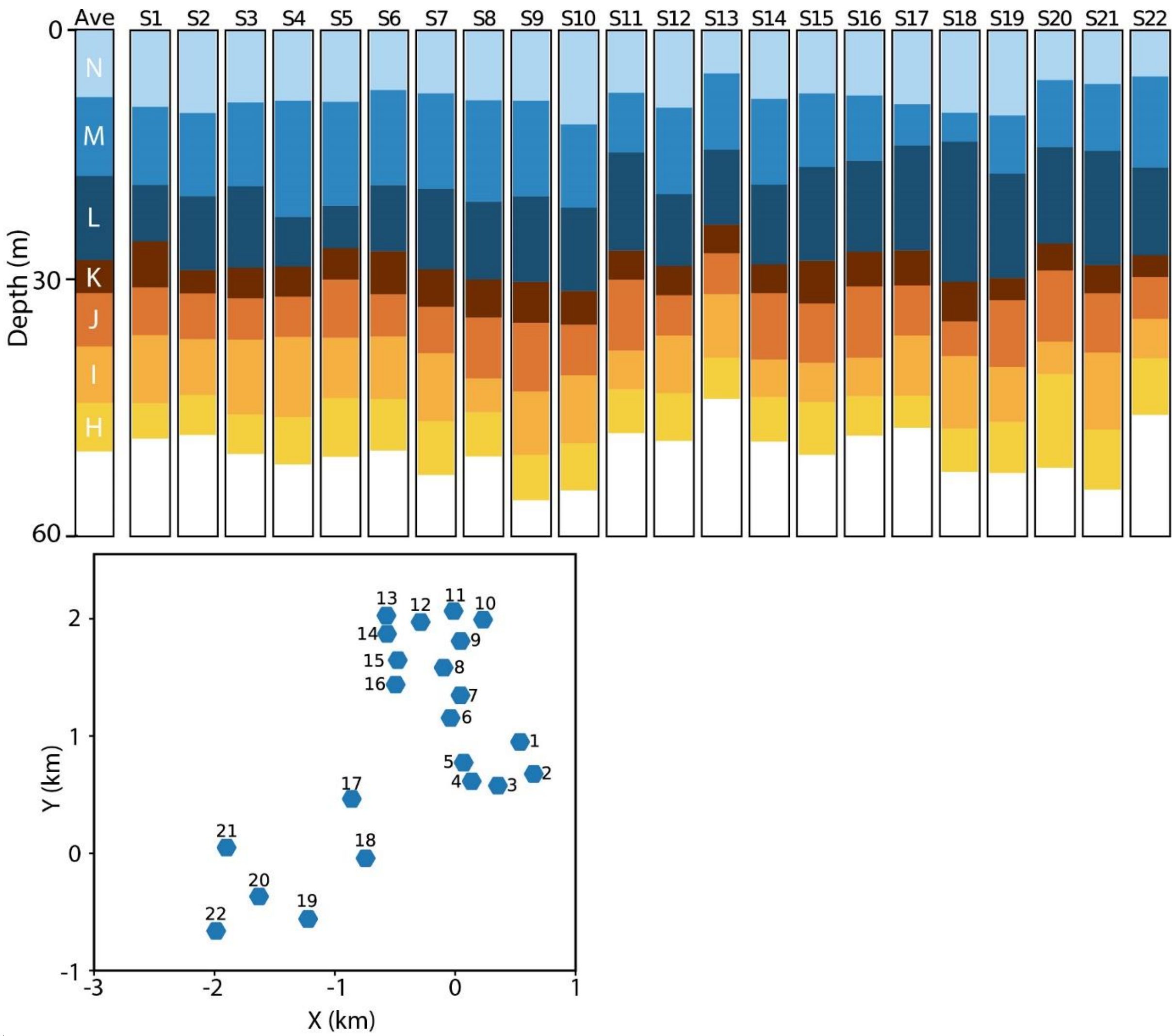

Figure 6. Variation of cycle thickness in the lateral extent. The lower panel shows locations of 22 digital sections, while the upper panel shows the thickness variations of seven successive cycles, with the top cycle flattened. Note that the coordinates in the lower panel are converted from global UTM coordinates to local ones, with the applied offset of X_offset = 673000 m and Y_offset = 49242600 m.

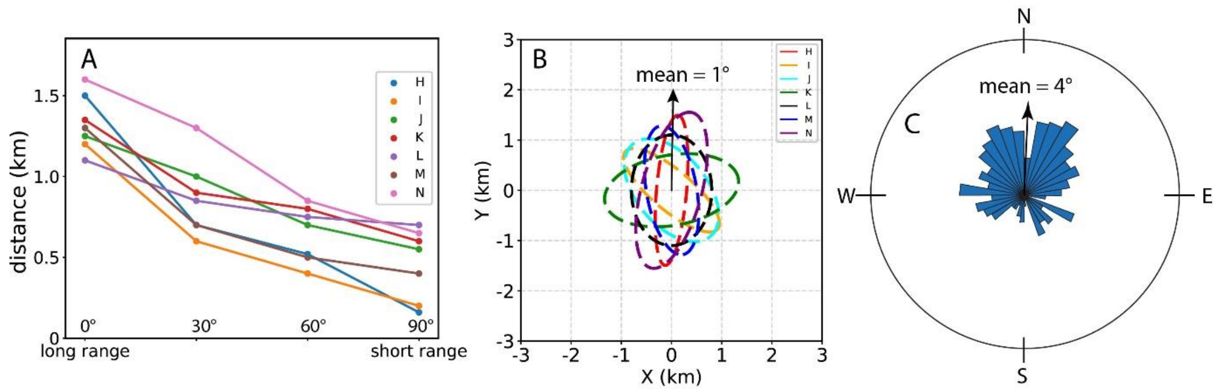

Figure 7. (A) Variation of ranges with azimuth, assuming the long-range azimuth to be 0° and thus the short-range azimuth to be 90°. (B) Oriented variogram ellipses with long and short ranges as long and short axes. (C) Field-measured paleoflow directions in the dune-scale cross-stratifications.

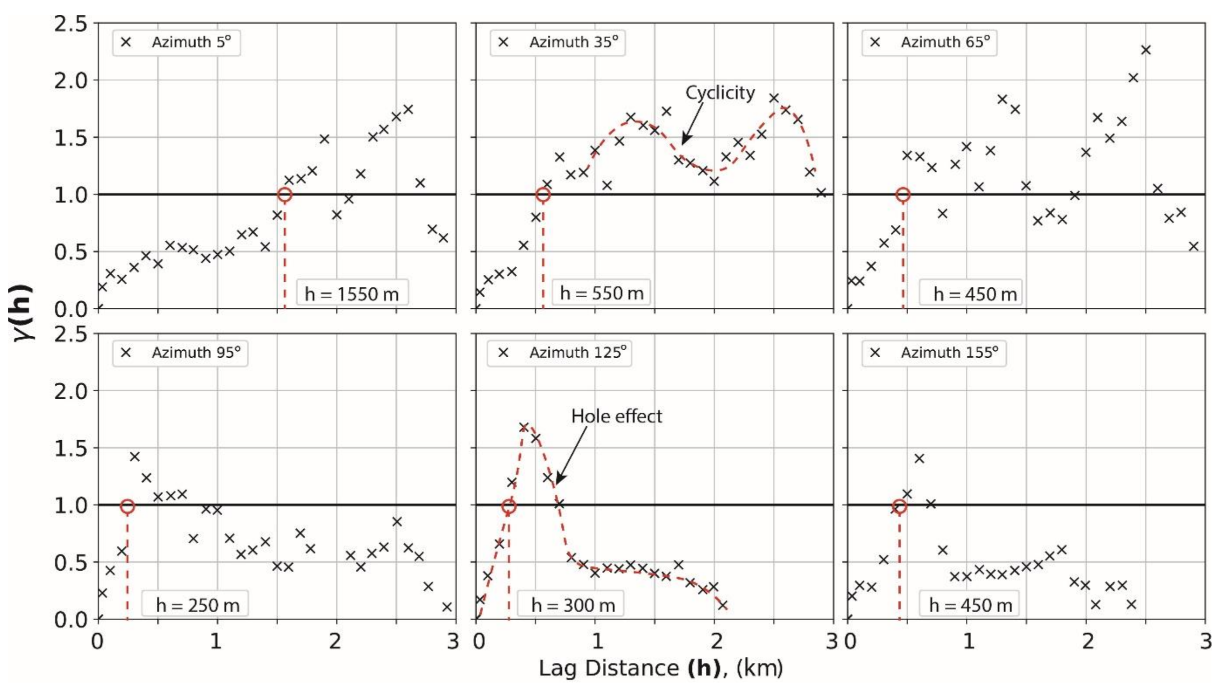

Figure 8. One-dimensional directional variograms for cycle H with different azimuths. Red circles and lines indicate the ranges along different azimuths. Information on how to read variograms has been detailed in Section 3.4.

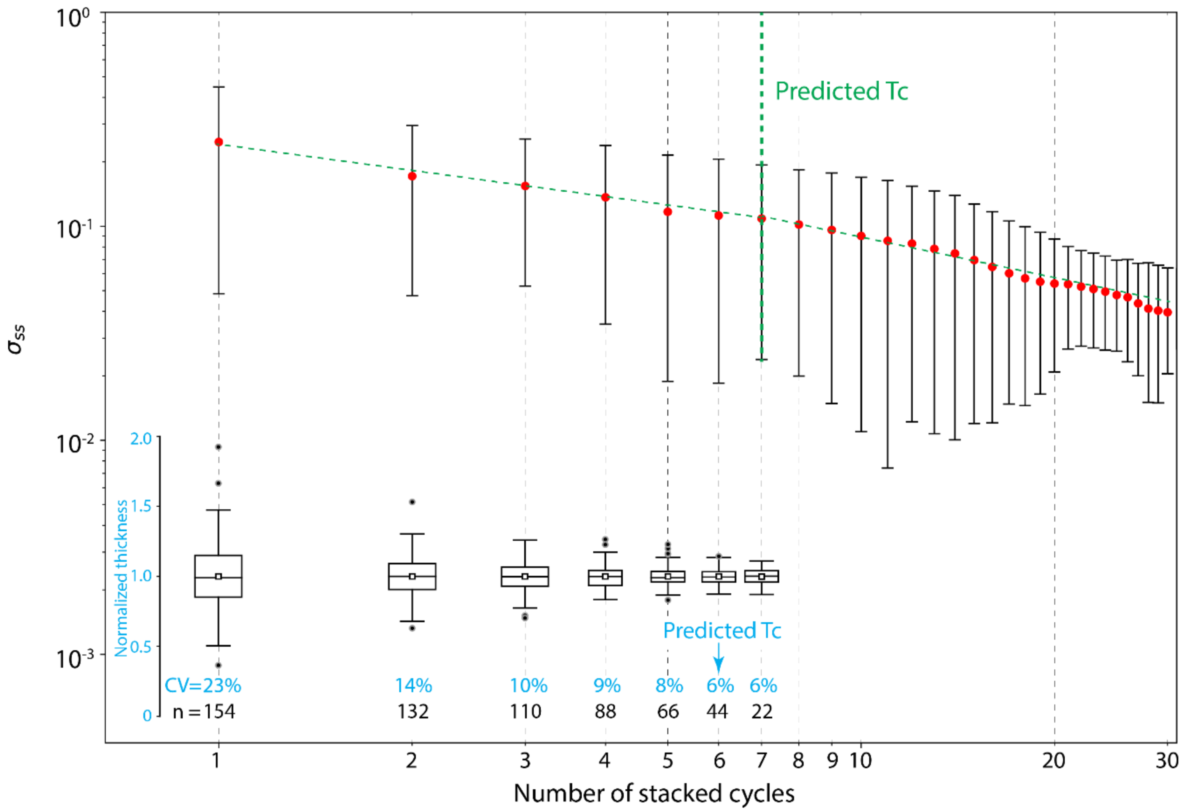

Figure 9. Two metrics for indicating the compensational timescale (Tc). (1) The lower part shows the decay of CV of the thicknesses of seven cycles with an increasing number of cycles. The predicted Tc corresponds to about 6 cycles since CV doesn't reduce anymore after the number of stacked cycles reaches 6. (2) The upper part shows the decay of σ_{ss} with an increasing number of cycles in the composite section (Figure 6). Error bars represent the geometric standard deviation, red dots indicate the average σ_{ss} at the corresponding number of cycles, green dashed trend lines represent best-fit linear, and the vertical green dashed line indicates the predicted Tc (see Straub et al., 2009 and Section 3.5.2 for a more detailed explanation of the principle) that corresponds to 7 cycles, over which the stratigraphic stacking transits from anti-compensational to compensational form.

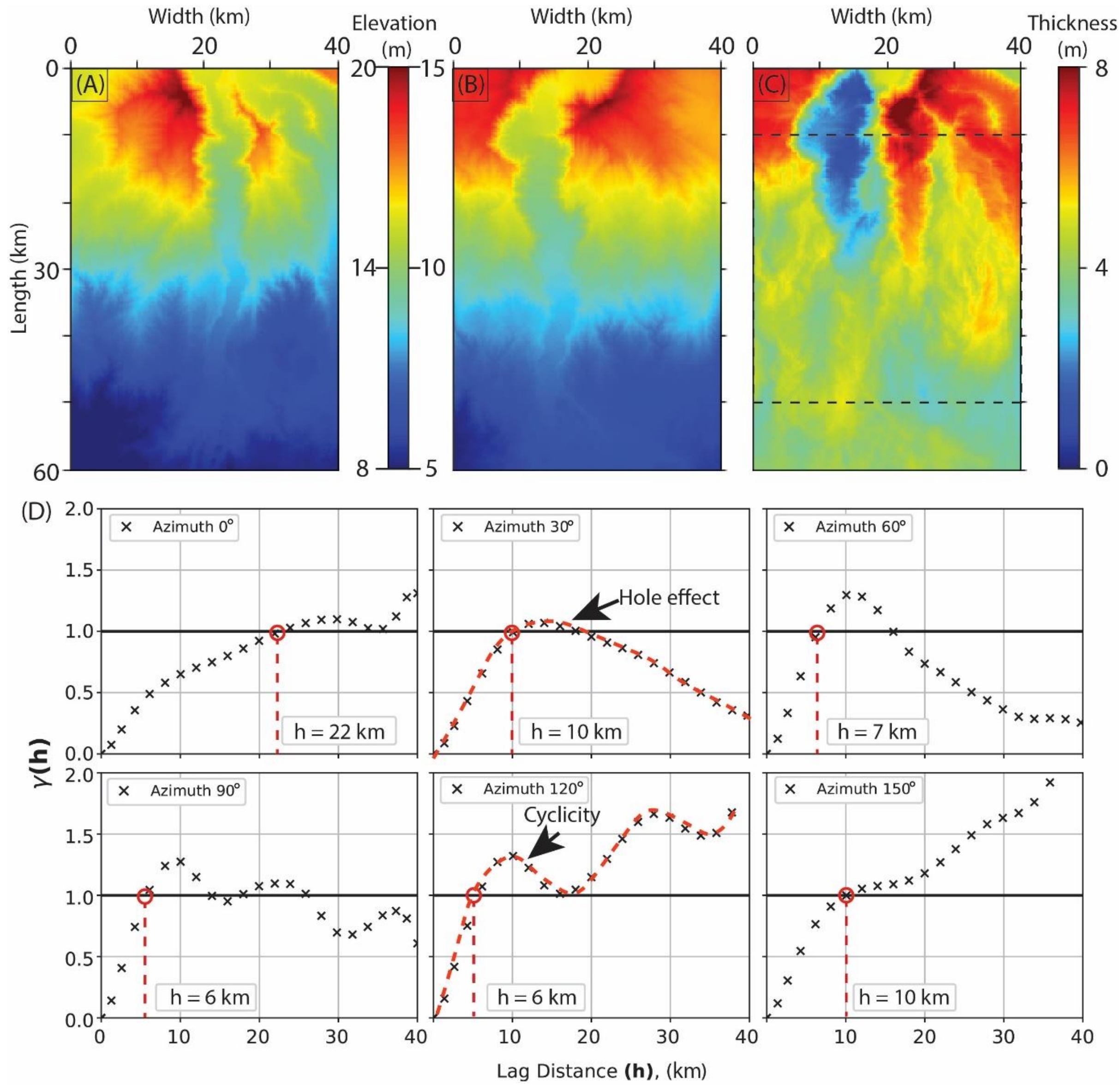

Figure 10. Geostatistical analysis using the Scenario A40 data produced by Wang *et al.* (2021). (A) The elevation map of the base of cycle 3. (B) The elevation map of the top of cycle 3. (C) The thickness map of cycle 3. (D) Directional variograms using the data constrained in the red rectangular of Figure 13C.

Appendix figures and tables

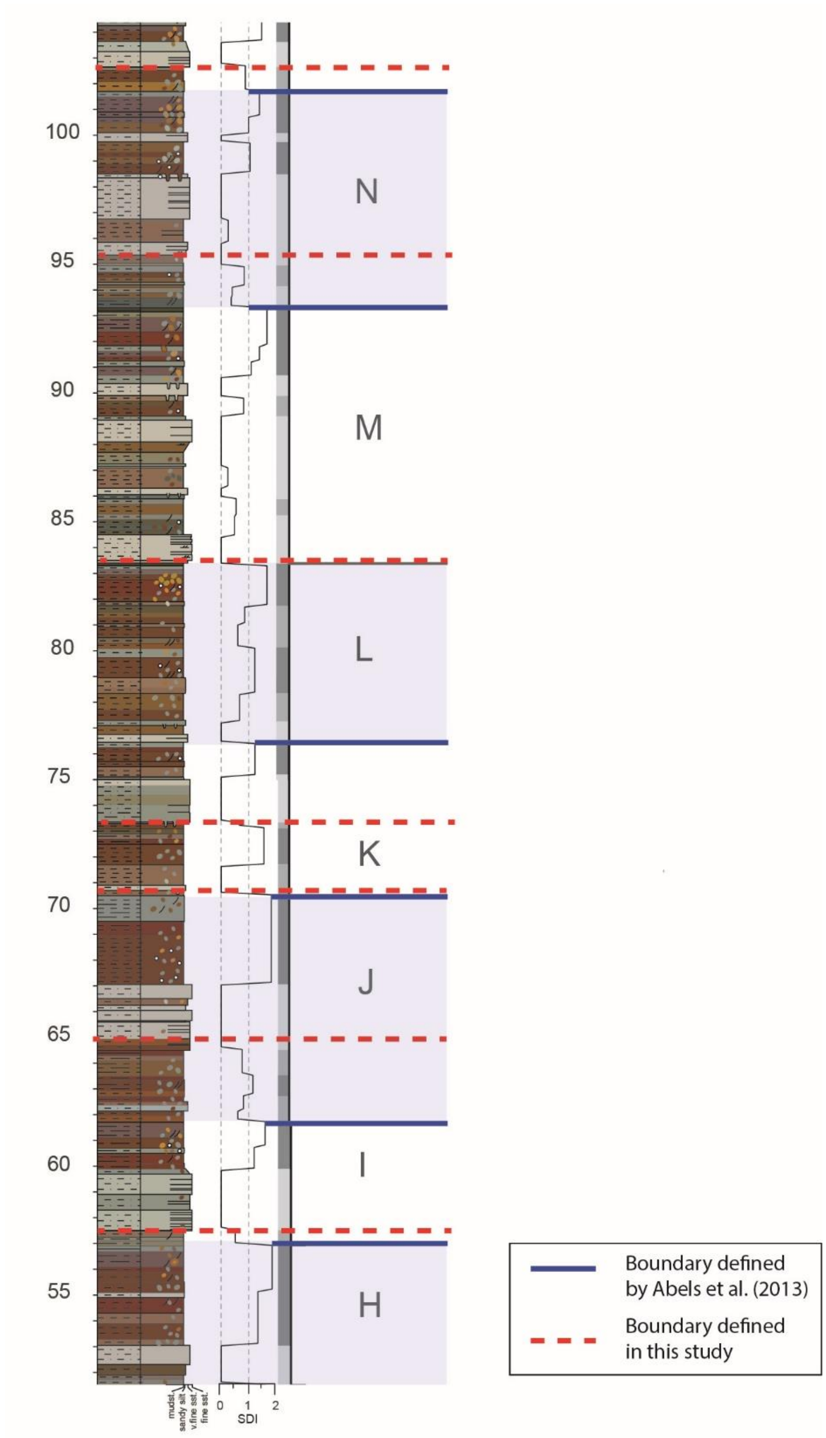

Figure S1. Comparison between FAC boundary in this study (red dash line) and that in Abels *et al.* (2013) (blue solid line), taking cycles H-N as examples.

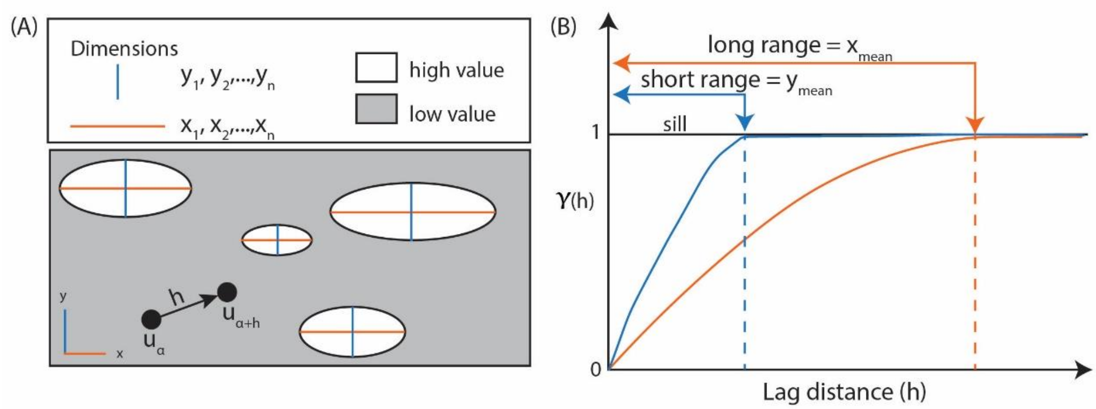

Figure S2. Schematic illustration of variogram components (modified from Pyrcz & Deutsch, 2003). (A) There are lenses with high values in the low-value background, with various long axes (x_1, x_2, …, x_n, averaging x_{mean}) and short axes (y_1, y_2, …, y_n, averaging y_{mean}); (B) The long and short ranges corresponding to x_{mean} and y_{mean} of high-value lens in Figure 4A, and observations appear independent (i.e. variance no longer increases) when the lag distance is beyond the range.

Table S1. Geostatistic features of thicknesses of different FACs

Cycle ID	Short range (km)	Long range (km)	Aspect ratio	Long-range azimuth
N	0.6	1.6	2.7	15°
M	0.5	1.3	2.6	350°
L	0.8	1.1	1.4	5°
K	0.7	1.4	2.0	80°
J	0.7	1.2	1.7	320°
I	0.4	1.2	3.0	310°
H	0.3	1.6	5.3	5°
Average	0.6	1.3	2.2	1°